Frequency locking and controllable chaos through exceptional points in optomechanics

P. Djorwe, Yan Pennec, Bahram Djafari-Rouhani

Frequency locking and controllable chaos through exceptional point in optomechanics

P. Djorwe,[1,*] Y. Pennec,[1,†] and B. Djafari-Rouhani[1,‡]

[1] *Institut d'Electronique, de Microélectronique et Nanotechnologie, UMR CNRS 8520 Université de Lille, Sciences et technologies, Villeneuve d' Ascq 59652, France*

We engineer mechanical gain (loss) in system formed by two optomechanical cavities (**OMCs**), that are mechanically coupled. The gain (loss) is controlled by driving the resonator with laser that is blue (red) detuned. We predict analytically the existence of multiple exceptional points (**EPs**), a form of degeneracy where the eigenvalues of the system coalesce. At each **EP**, phase transition occurs, and the system switches from weak to strong coupling regimes and vice versa. In the weak coupling regime, the system locks on an intermediate frequency, resulting from coalescence at the **EP**. In strong coupling regime, however, two or several mechanical modes are excited depending on system parameters. The mechanical resonators exhibit Rabi-oscillations when two mechanical modes are involved, otherwise the interaction triggers chaos in strong coupling regime. This chaos is bounded by **EPs**, making it easily controllable by tuning these degeneracies. Moreover, this chaotic attractor shows up for low driving power, compared to what happens when the coupled **OMCs** are both drived in blue sidebands. This works opens up promising avenues to use **EPs** as a new tool to study collective phenomena (synchronization, locking effects) in nonlinear systems, and to control chaos.

PACS numbers: 42.50.Wk, 42.50.Lc, 05.45.Xt, 05.45.Gg
Keywords: Optomechanics, exceptional point, frequency locking, chaos

I. INTRODUCTION

Optomechanical systems provide a promising platform to explore light-matter interactions for both technological applications and fundamental physics [1]. Through optomechanics, a mechanical resonator can be studied from quantum ground state [2],[3],[4] to the amplified regime characterized with large displacements [5],[6],[7].

At the parametric instability point, where the backaction-induced mechanical gain overcomes mechanical loss, mechanical self-oscillations start [8], [9],[10], and the system enters into a nonlinear regime. This regime is a prerequisite to study collective phenomena such as synchronization and frequency locking [11],[12],[13],[14],[15]. Such phenomena have practical applications in rf communication [16], signal-processing [17], clock synchronization [18] and novel computing and memory concepts [19]. In [13], two lasers were used to lock two optomechanical systems, while the all-optical light-mediated locking of three spatially distant optomechanical oscillators was achieved using a single laser source in [15]. The threshold of this locking effect as well as the mechanism behind it are not well predicted, but occurs spontaneously as the driving strength is increasing [13], [15]. Therefore, predictability and controllability of locking phenomenon become relevant.

In optomechanics, it is well-known that strong driving strength induces period doubling and chaos [20],[21],[22], [23]. Chaotic behaviour is useful for generating random numbers and implementing secret information processing (see [24] and references therein). However, to apply chaos into a secret communication scheme, good controllability and low-power threshold are required [25],[26]. Low-driving threshold chaos has been achieved in [25], using optical PT-symmetry in an optomechanical system; while controllable chaos with a low-driving threshold has been investigated in an electro-optomechanical system in [26]. A system that can handle these issues concerning locking phenomenon and chaos, would be a good benchmark for technological applications based on nonlinear optomechanics.

Here, we investigate a system that provides both controllability and low-power threshold for chaos as well as the predictability and control of frequency locking phenomenon. The key point of this is the exceptional points (**EPs**), a form of degeneracy in gain and loss systems, where the eigenvalues coalesce and become conjugate complex numbers [27]. The proposal system is formed by two **OMCs**, that are mechanically coupled. The gain and loss are created by symmetrically driving the cavities with blue and red detuned lasers, respectively. Interesting counter-intuitive features and intriguing effects such as stopping light [28], loss-induced suppression and revival of lasing, pump-induced lasing death, and unidirectional invisibility have been observed in the vicinity of **EPs** (see [29] and references therein). Owing to these interesting properties of **EPs**, here we show that: (i) chaos and multistability vanish at the **EP** and (ii) frequency locking effect is induced by **EP**. This dual effect results from the coalescence of modes. Therefore, switching from multimode to single mode scrucially depends on the **EP**. These results pave a way to control chaos and to predict locking effects in large-scale networks of nonlinear systems by exploiting **EPs**. This work is organized as follows. In Sec. II, the system and the dynamical equa-

*Electronic address: philippe.djorwe@univ-lille1.fr
†Electronic address: yan.pennec@@univ-lille1.fr
‡Electronic address: bahram.djafari-rouhani@@univ-lille1.fr

tions are described. The predictability of frequency locking effect and control of chaos are presented in Sec. III. Section IV is devoted to investigate the transient chaotic behaviour and out of phase synchronization, while Sec. V concludes the work.

II. MODELLING AND DYNAMICAL EQUATIONS

The system of our proposal is the one in Fig. 1a, where the cavity labelled 1 (labelled 2), is driven with a red (blue) detuned laser. In the rotating frame of the driving fields, the Hamiltonian ($\hbar = 1$) describing this system is,

$$H = H_{OM} + H_{int} + H_{drive}, \tag{1}$$

with

$$\begin{cases} H_{OM} = \sum_{j=1,2}[-\Delta_j a_j^\dagger a_j + \omega_{0j} b_j^\dagger b_j - g a_j^\dagger a_j (b_j^\dagger + b_j)] \\ H_{int} = -J(b_1 b_2^\dagger + b_1^\dagger b_2) \\ H_{drive} = \sum_{j=1,2} E(a_j^\dagger + a_j). \end{cases} \tag{2}$$

In this Hamiltonian, ω_{0j} ($\omega_{01} \neq \omega_{02}$) and $\Delta_j = \omega_p^j - \omega_{cav}^j$ are the mechanical frequency of the j^{th} resonator and the optical detuning between the j^{th} optical drive (ω_p^j) and the j^{th} cavity eigenfrequency (ω_{cav}^j), respectively. The quantities a_j and b_j are the annihilation bosonic field operators describing the optical and mechanical resonators, respectively. The mechanical displacements x_j are connected to b_j as $x_j = x_{\rm ZPF}(b_j + b_j^\dagger)$, where $x_{\rm ZPF}$ is the zero-point fluctuation amplitude of the mechanical resonator. The mechanical coupling strength between the two mechanical resonators is J, and the optomechanical coupling is g. The amplitude of the driving pump is E. The quantum Langevin equations (QLEs) for the operators of the optical and the mechanical modes are derived from Eq. (2) as,

$$\begin{cases} \dot{a}_j = [i(\Delta_j + g(b_j^\dagger + b_j)) - \frac{\kappa}{2}]a_j - i\sqrt{\kappa}(a^{in} + \xi_{a_j}), \\ \dot{b}_j = -(i\omega_{0j} + \frac{\gamma_m}{2})b_j + iJb_{3-j} + iga_j^\dagger a_j + \sqrt{\gamma_m}\xi_{b_j}, \end{cases} \tag{3}$$

where optical (κ) and mechanical (γ_m) dissipations have been added, and the amplitude of the driving pump has been substituted as $E = \sqrt{\kappa}a^{in}$ in order to account for losses. In this form, the input laser power $\rm P_{in}$ acts through $a^{in} = \sqrt{\frac{\rm P_{in}}{\hbar\omega_p}}$. The term ξ_{a_j} (ξ_{b_j}) denotes the optical (thermal) Langevin noise at room temperature.

We seek to investigate in the classical limit, where photon and phonon numbers are assumed large in the system, and noise terms can be neglected in our analysis. Thus, we rewrite Eq. (3) into a set of differential equations for the four complex scalar fields, $\{\alpha_j\}_{j=1,2}$ for the optics and $\{\beta_j\}_{j=1,2}$ for the mechanics, standing for the mean values of the operators $\langle a\rangle = \alpha_j$ and $\langle b\rangle = \beta_j$. This leads to the following set of nonlinear equations,

$$\begin{cases} \dot{\alpha}_j = [i(\Delta_j + g(\beta_j^* + \beta_j)) - \frac{\kappa}{2}]\alpha_j - i\sqrt{\kappa}\alpha^{in}, \\ \dot{\beta}_j = -(i\omega_{0j} + \frac{\gamma_m}{2})\beta_j + iJ\beta_{3-j} + ig\alpha_j^*\alpha_j, \end{cases} \tag{4}$$

For simplicity, the parameters (γ_m, g, κ) are assumed to be degenerated for both cavities. Throughout the work, we assume the hierarchy of parameters $\gamma_m, g \ll \kappa \ll \omega_{0j}$, similar to the experiments carried out in the resolved sideband regime [30],[31].

In Figs. 1(b)−(e), we show the overall properties of the steady state solutions of Eq. (4), where all the transient dynamics has died out. Three regimes can be identified in (α^{in}, J) parameter's space. As the driving α^{in} increases for a fixed $J = 2.2\times10^{-2}\omega_m$ (see dashed line in Fig. 1b), the system switches from the linearized regime (blue area) to the nonlinear one (gray and green colors) through the onset of the self-induced oscillations. In the nonlinear regime, the system switches twice into weak coupling regimes (gray color), and once into a strong coupling regime (green color). The meaning of weak (strong) coupling regime will be given later on. Each transition in weak coupling regime is followed by limit cycle oscillations, and both mechanical resonators lock and start oscillating with a common frequency (see Fig. 1c). However, this frequency locking phenomenon is destroyed when the system jumps into the strong coupling regime, where Rabi oscillations show up (see Fig. 1d and Fig. 1e). These Rabi oscillations can be regular (Fig. 1d) or chaotic like-behaviour (Fig. 1e and light green area in Fig. 1b). This chaotic attractor is bounded between two limit cycle regimes. Such phase transitions, between weak and strong couplings in coupled gain/loss system, are reminiscent of **EP** [32],[33]. It results that, (i) our system features multiple **EPs** [34], which are useful: (ii) to induce frequency locking, (iii) and to control chaotic dynamics.

To get insight of the **EP** features, we approach the limit cycle oscillations by the ansatz, $\beta_j(t) = \bar{\beta}_j + A_j\exp(-i\omega_{\rm lock}t)$ [35]. $\bar{\beta}_j$ is a constant shift in the origin of the movement, A_j is the slowly time dependent amplitude of the cycles, and $\omega_{\rm lock}$ is the mechanical locked frequency. Similar to multistability in optomechanics [35], this ansatz aims to provide analytical tools, describing the feature of multiple **EPs**. Using this ansatz, it is straightforward to integrate $\alpha_j(t)$ out of the full system (see Appendix B), resulting in effective equations of motion for just the mechanical resonators having the form $i\partial t\Psi = H_{eff}\Psi$. We have set the state vector $\Psi = (\beta_1, \beta_2)^T$ and the effective Hamiltonian is,

$$H_{eff} = \begin{bmatrix} \omega_{eff}^1 - i\frac{\gamma_{eff}^1}{2} & -J \\ -J & \omega_{eff}^2 - i\frac{\gamma_{eff}^2}{2} \end{bmatrix}. \tag{5}$$

This Hamiltonian has the eigenvalues,

$$\lambda_\pm \simeq \frac{\omega_{eff}^1 + \omega_{eff}^2}{2} - \frac{i}{4}\left(\gamma_{eff}^1 + \gamma_{eff}^2\right) \pm \frac{\sigma}{2}. \tag{6}$$

Here $\omega_{eff}^j = \omega_{0j} + \delta\omega_j$ and $\gamma_{eff}^j = \gamma_m + \gamma_{opt}^j$ are the effective frequencies and dampings respectively. The quantity $\sigma \approx \sqrt{4J^2 - \frac{\Delta\gamma_{eff}^2}{4}}$, with $\Delta\gamma_{eff} = \gamma_{eff}^2 - \gamma_{eff}^1$, is

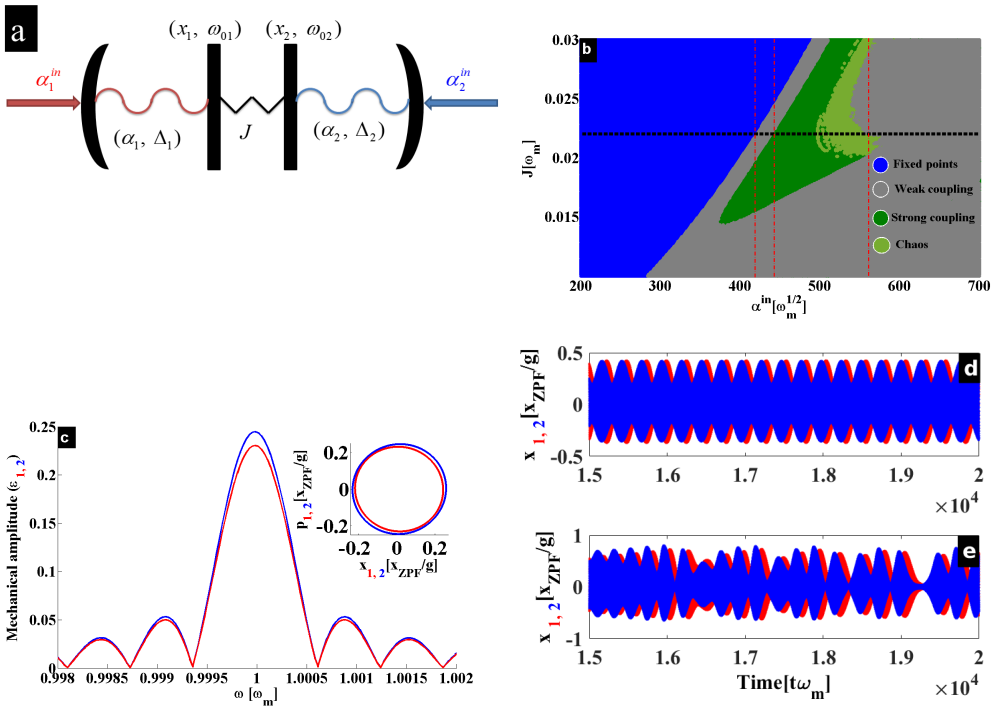

FIG. 1: (a) Generic setup. (b) Numerical diagram depicting the possible regimes involved. (c) Locked frequency and its corresponding phase space representation (see inset, p is the momentum). (d) and (e) Regular and chaotic Rabi oscillations, respectively. Blue (red) color is related to the blue (red) mechanical supermode. In (c)-(e), $J = 2.2 \times 10^{-2}\omega_m$ and $\alpha^{in} = (4.3\times10^2, 4.5\times10^2, 5.5\times10^2)\sqrt{\omega_m}$ respectively. The other used parameters are, $\gamma_m = 10^{-3}\omega_m$, $\kappa = 10^{-1}\omega_m$, $g = 2.5\times10^{-4}\omega_m$, $\omega_{01} = 1.002\omega_m$, $\omega_{02} = \omega_m$, $\Delta_1 = -\omega_m$ and $\Delta_2 = \omega_m$.

amplitude dependent through the normalised amplitude $\epsilon_j = \frac{2g\mathrm{Re(A_j)}}{\omega_{\mathrm{lock}}}$. Indeed, the optical dampings γ_{opt}^j are expressed as ,

$$\gamma_{opt}^j = \frac{2(g\kappa\alpha^{in})^2}{\epsilon_j}\sum_n \frac{J_{n+1}\left(-\epsilon_j\right)J_n\left(-\epsilon_j\right)}{\left|h_{n+1}^{j*}h_n^j\right|^2}, \qquad (7)$$

where J_n is the Bessel function, $h_n^j = i\left(n\omega_{\mathrm{lock}} - \tilde{\Delta}_j\right) + \frac{\kappa}{2}$ and $\tilde{\Delta}_j = \Delta_j + \delta_j$, with $\delta_j = 2g(\bar{\beta}_j)$, is the nonlinear detuning (see Appendix B). The eigenfrequencies and the dampings of the system are defined as the real ($\omega_\pm = \Re(\lambda_\pm)$) and imaginary ($\gamma_\pm = \Im(\lambda_\pm)$) parts of $\lambda_\pm$, respectively. However, the quantities $\omega_\pm$ and $\gamma_\pm$ depend on σ, delimiting the weak and strong regimes aforementioned in Fig. 1b. The strong coupling regime is defined for $J > \frac{\Delta\gamma_{eff}}{4}$, while the weak coupling one holds for $J < \frac{\Delta\gamma_{eff}}{4}$. The **EPs**, phase transitions between these two regimes, are defined by $J = \frac{\Delta\gamma_{eff}}{4}$. This induces $\sigma = 0$, whose solutions predict multiple **EPs** [34], owing to the oscillating nature of σ (see the dashed line in Fig. 1b). After demonstrating the emergence of multiple **EPs**, we take a step further, showing that **EPs** can be used as a new paradigm both for achieving frequency locking and to control chaos.

III. FREQUENCY LOCKING AND CHAOS

A. Frequency locking

In the linear regime, $\epsilon_j \to 0$, we use $\{\sigma(\epsilon_j), \mu(\epsilon_j)\} \to \{\sigma_0, \mu(0)\}$, where μ stands for any amplitude-dependent term. The mechanical resonators oscillate with two eigenfrequencies (see Fig. 2a),

$$\omega_\pm \simeq \frac{\omega_{eff}^1(0) + \omega_{eff}^2(0)}{2} \pm \frac{\sigma_0}{2}, \qquad (8)$$

that exchange energy through Rabi oscillations [32],[33] as depicted in the inset of Fig. 2a. These Rabi oscillations have an exponentially decaying profile whose is defined by the imaginary parts of the eigenvalues (see Fig. 2b),

$$\gamma_\pm = \frac{-\left(\gamma_{eff}^1(0) + \gamma_{eff}^2(0)\right)}{4}. \qquad (9)$$

The quantity $\Delta\gamma_{eff}$ is quadratic in α^{in} (see Eq. (7)), and it will overcome $4J^2$ as α^{in} is increasing, that is at $\mathbf{EP}_1$. Consequently, the two mechanical resonators spontaneously lock at the frequency $\omega_{\text{lock}} = \frac{\omega^1_{eff}+\omega^2_{eff}}{2}$, as it can be deduced from Eq. (8). This locking effect persists until another **EP** is reached. This constitutes one of our findings, showing that frequency locking is achieved through **EP**. This result opens up novel prospects for applications of **EPs** in realizing locking modes in optomechanics and others similar devices.

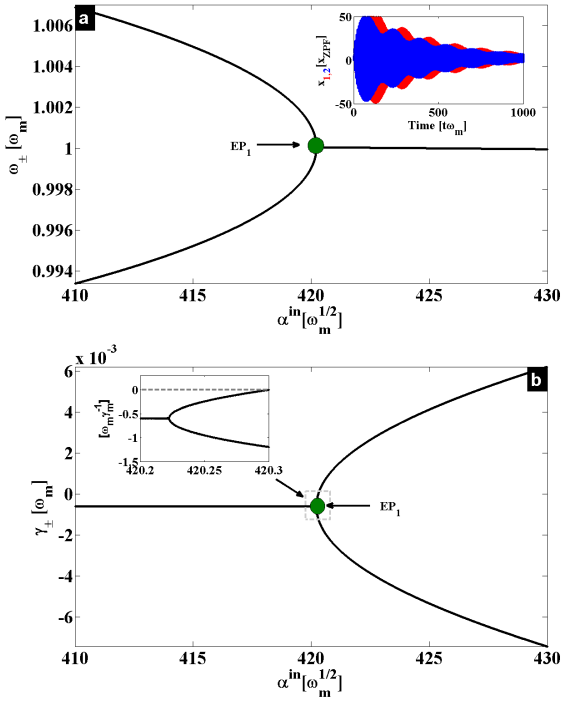

FIG. 2: (a), (b) Real and imaginary part of the eigenmodes, respectively. Inset of (a) shows (mechanical) Rabi oscillations at $\alpha^{in} = 3 \times 10^2\sqrt{\omega_m}$. The coupling strength is $J = 2.2 \times 10^{-2}\omega_m$ and the other parameters are as in Fig. 1.

B. Chaos

In the nonlinear regime, linear approximation is preserved for weak amplitudes ($\epsilon_j \ll 1$) [30],[36], and both dissipations ($\gamma_\pm$) keep the same sign (see inset of Fig. 2b). For non-negligible ϵ_j, the oscillations of σ can lead to multiple **EPs**. For $J = 2.2 \times 10^{-2}\omega_m$ for instance, $\mathbf{EP}_2$ and $\mathbf{EP}_3$ are induced as shown in Fig. 3a and Fig. 3b (see also vertical and horizontal line intersections in Fig. 1b). Weak coupling holds between $\mathbf{EP}_1$ and $\mathbf{EP}_2$. Beyond $\mathbf{EP}_2$, the system jumps into a strong coupling regime, where Rabi oscillation emerge (see Fig. 1d). As the driving increases, the optical nonlinearity δ_j splits into multistable solutions (see Fig. 3a), affecting the frequency of Rabi oscillations σ. In our proposal, this multistability process constitutes a route to chaos [23]. When the optomechanical nonlinearities become comparable to the optical linewidth ($\delta_j \sim \frac{\kappa}{2}$), chaotic oscillations are triggered in the system. This can be seen in Fig. 3b, showing range of frequencies continuum. This figure is obtained by collecting peaks and corresponding frequencies, of the mechanical steady states, from Fast Fourier Transform (FFT). Such bifurcation diagram in frequency space is useful here, since it has the advantage of well-tracking dynamics of Rabi oscillations (see Appendix A). Through Lyapunov Exponent (**LE**) [24],[25], we have confirmed this chaotic behaviour in Fig. 3c. The negative (positive) value of **LE** indicates that the system exhibits periodic (chaotic) dynamics. For quasi-periodic behaviour, discrete frequencies in Fig. 3b, **LE** is close to zero. As the driving strength is growing, $\mathbf{EP}_3$ is reached, and the system switches back into the weak coupling regime. Features stemming from the presence of $\mathbf{EP}_3$ are the disappearance of Rabi oscillations [32] and the spontaneous emergence of frequency locking (see Fig. 3b for $\alpha^{in} \sim 5.6 \times 10^2\sqrt{\omega_m}$). It results that, the chaotic attractor is bounded between $\mathbf{EP}_2$ and $\mathbf{EP}_3$. Threshold of this chaos can be controlled by tuning **EPs** through system's parameters. We focus our investigation here on the mechanical frequency mismatch $\omega_{01} - \omega_{02}$. The reason lies on the difficulties to engineer two identical mechanical resonators, that have exactly the same frequencies. For a fixed $J = 2.2 \times 10^{-2}\omega_m$, Fig. 3d shows that, the mechanical resonators can be no longer strongly coupled if their frequency mismatch exceeds $(\omega_{01} - \omega_{02}) \gtrsim 10^{-2}\omega_m$. Furthermore, large frequency mismatch destroys chaotic dynamics, since chaos is limited for $(\omega_{01} - \omega_{02}) \lesssim 5 \times 10^{-3}\omega_m$ as shown by the light green color in Fig. 3d. It follows that, an increase (decrease) of the mechanical frequency mismatch controls (induces) chaotic dynamics. Conversely, increasing $(\omega_{01} - \omega_{02})$ enhances frequency locking effect. This provides a method of manipulating and controlling chaos through **EPs**, making it useful in large technological platforms [23]. This is our second finding, suggesting a bounded and controllable chaos through **EPs** in coupled **OMCs**. The main ingredient for the emergence of this chaos is a strong coupling between the mechanical resonators, instead of being a strong driving strength [20],[21],[22], [23].

In the above discussion, we considered the blue-red configuration of coupled cavities. For a matter of comparison, the inset of Fig. 3c shows the **LE** obtained in the analog blue-blue configuration, using the same parameters. It results that, the threshold of chaos is reduced almost four times in our proposal (see also [24], [25]). Lowering threshold of chaos is a requiring element in a secret communication scheme, and our work provides a new paradigm based on tunability of **EP**.

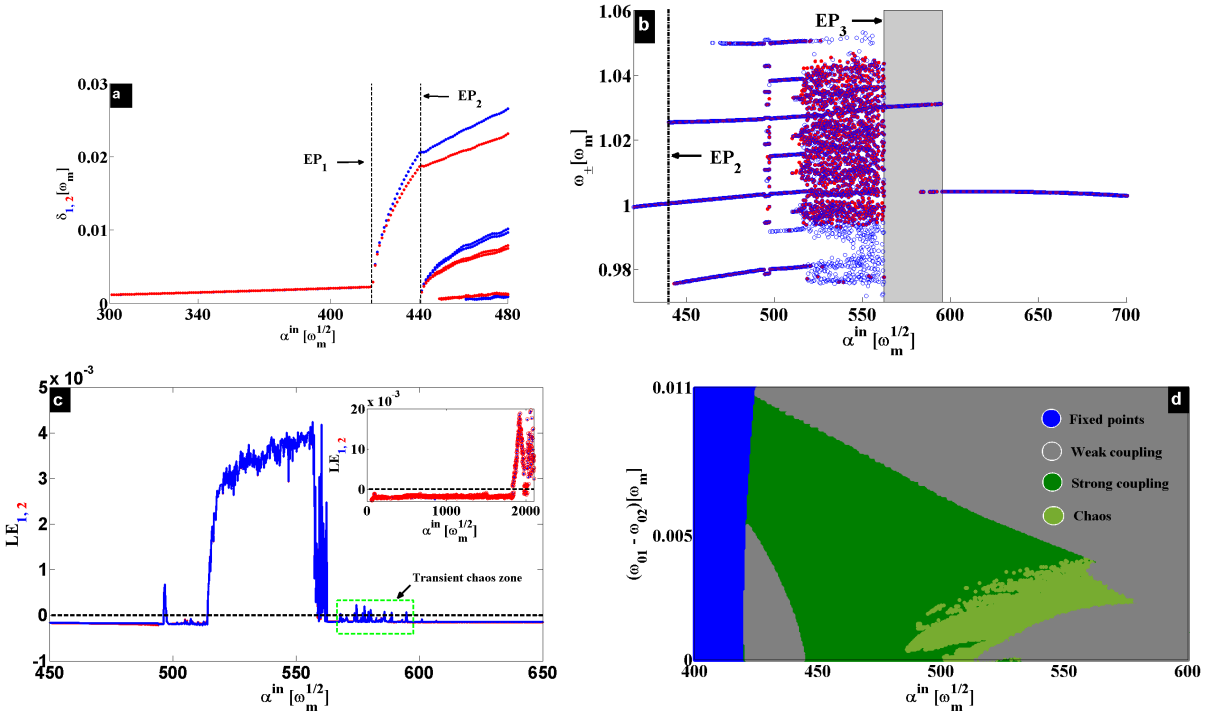

FIG. 3: (a) Frequency shift and origin of nonlinearities. (b) Frequencies of the mechanical resonators versus α^{in}. (c) Corresponding Lyapunov Exponent (**LE**) versus α^{in}. The inset of (c) is the **LE** for the analog blue−blue configuration. (d) Overview of dynamical states related to frequency mismatch $\omega_{01} - \omega_{02}$ at $J = 2.2 \times 10^{-2}\omega_m$.

IV. TRANSIENT CHAOS AND π-SYNCHRONIZATION

A. Transient chaos

The phenomenon of transient chaos was recently studied in optomechanics [39]. Besides being a physically meaningful phenomenon by itself, these authors have shown that transient chaos constitutes a bridge for the quantum-classical transition. However, we show here that transient chaos induces transition towards frequency locking. At the $\mathbf{EP}_3$, chaotic dynamics vanishes, and the system locks back at ω_{lock} (see Fig. 3b). This locked state depends on whether there is a coexistence between transient chaos and limit cycle attractors or not. In the former case, this coexistence locks the system on a higher energy state, otherwise the locking is achieved on the lower energy state. As we can see in the gray area in Fig. 3b, the system starts on the upper branch (higher energy), and gradually switches on the lower branch (lower energy) as the driving strength is increasing. This is depicted in Fig. 4, where we have chosen two values of α^{in}, one for the upper branch (see Fig. 4a) and the other on the lower branch (see Fig. 4b). It results that, transient chaos and limit cycle attractors coexist on the upper branch, while Rabi-oscillations precede limit cycles on the lower branch. When transient chaos is involved, the **LE** starts diverging, and decays over time in order to match the appropriate limit cycle dynamics. However, this relaxation time is long that the chaotic signature persists in the **LE** (see the green box in Fig. 3c). As the configuration in Fig. 4b is more stable than the one in Fig. 4a [39], after a short competition between upper and lower branches, the system finally settles into the lower branch that is more stable. Besides its dynamical aspect, the transient state determines the kind of collective phenomenon exhibited by the final steady state (see zooms in Fig. 4a and Fig. 4b).

B. π-synchronization

Beyond this transient regime (gray area in Fig. 3b), only the locked state with the lower energy persists and the mechanical resonators exhibit two different behaviours based on their phase difference. Either they oscillate out of phase or they exhibit limit cycle oscillations with different dissipations,

$$\gamma_{\pm} = \frac{-\left(\gamma_{eff}^{1} + \gamma_{eff}^{2}\right)}{4} \pm \frac{\sigma}{2}. \tag{10}$$

In the latter case, the asymmetry between the dissipation rates ($|\gamma_-| \neq |\gamma_+|$) induces unidirectional flow of phonons [37], [38] between the resonators as shown

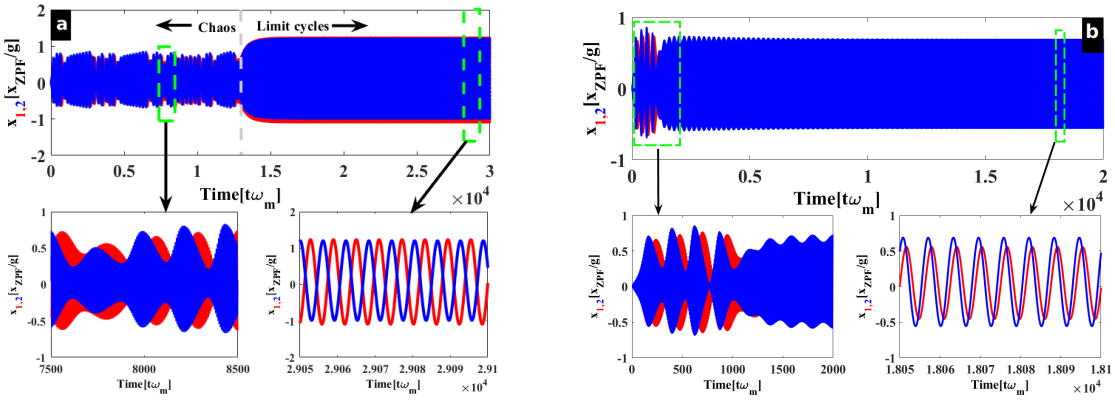

FIG. 4: (a) Transient chaos induced π-synchronization at $\alpha^{in} = 5.7 \times 10^2\sqrt{\omega_m}$. (b) Frequency locking with transient Rabi-oscillations at $J = 5.9 \times 10^{-3}\omega_m$. (a)-(b) correspond to the coupling strength $J = 2.2 \times 10^{-2}\omega_m$.

in Fig. 5a. However, the first case happens when $\gamma^1_{eff} \sim -\gamma^2_{eff}$, leading to $\gamma_\pm \sim \pm\frac{\sigma}{2}$ [33]. Consequently, the mechanical resonators carry out approximately broken $\mathcal{PT}-$symmetry dynamics, resulting in a $\pi-$synchronization ($\Delta\phi = \phi_1 - \phi_2 = \pi$) as a signature. This is shown in Fig. 5b, where the standard deviation of $\Delta\phi$ is represented. The phase is defined as being $\tan(\phi_j) = \frac{\mathrm{Im}(\beta_j)}{\mathrm{Re}(\beta_j)}$, confirming the phase difference of π when $\gamma_\pm \sim \pm\frac{\sigma}{2}$.

The parameters we have used here are similar to those in the recent experiments [30], [31]. This offers the prospects to experimentally reproduce the present results. Moreover, this study can be extended to a wide variety of optomechanical systems, including hybrid optical-microwave setups and electromechanical systems. Our findings do not necessarily need $\mathcal{PT}-$symmetry, and the resonators can have different frequencies (see Fig. 3d).

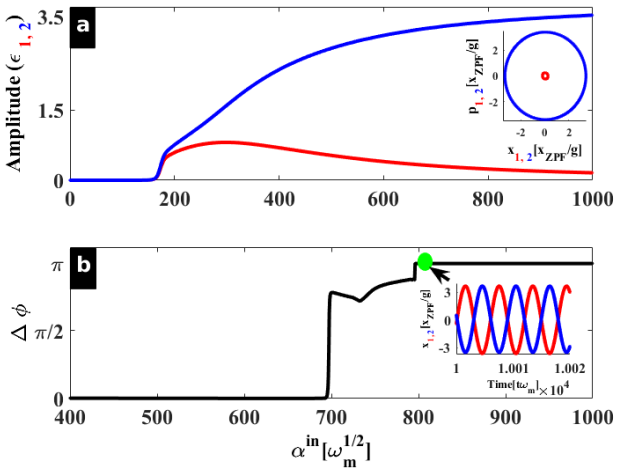

FIG. 5: (a) Asymmetric dissipation at $J = 5 \times 10^{-3}\omega_m$. (b) Standard deviation of $\delta\phi$ showing π-synchronization for $J = 6 \times 10^{-2}\omega_m$. The insets in (a) and (b) show limit cycle and time propagation at $\alpha^{in} = 8\times10^2\sqrt{\omega_m}$. The other parameters are as in Fig. 1.

V. CONCLUSION

In conclusion, we have studied two optomechanical systems that are mechanically coupled. By driving the cavities, one by blue detuned laser and the other with a red detuned laser, we have respectively created gain and loss on these mechanical resonators. We have predicted analytically, the existence of multiple **EPs**. The system switches from weak to strong coupling regimes through these **EPs**. In the weaks coupling regimes, we demonstrated frequency locking effect induced by these degeneracies. In the strong coupling regime instead, we have shown that optical nonlinearities trigger chaos. This chaotic attractor is bounded between two **EPs**, providing an accurate way to control it by adjusting gain/loss parameters. This work offers the prospects to use **EPs** as a new tools for controlling and thresholdless chaos. Furthermore, **EPs** open up a promising route for realizing collective phenomena (locking effect, synchronization) in nonlinear devices.

Acknowledgments

This work was supported by the European Commission FET OPEN H2020 project PHENOMEN-Grant Agreement No. 713450.

Appendix A: Dynamical states

Numerical steady state solutions of Eq. (4) are shown by Fig.1b in the main text. Three dynamical states are depicted, the fixed point regime, the limit cycles regime, and the regime where Rabi oscillations emerge. The aim here is to characterize dynamically, the steady states solutions in these regimes. For this purpose, we have fixed $J = 2.2 \times 10^{-2}\omega_m$, where all these regimes are met by varying the driving strength α^{in} (see the horizontal dashed line in Fig.1b in the main text). Hence, time propagation of some steady state solutions are given in Fig. 6. Fixed point regime is shown in Fig. 6a, where Rabi oscillations are decaying with a same rate as explained in the main text. The frequency of these Rabi oscillations is σ_0, and the mechanical resonators are in strong coupling regime. Fig. 6b represents limit cycle oscillations at $\alpha^{in} = 4.3 \times 10^2\sqrt{\omega_m}$, and the system is in a weak coupling regime. Figs. 6(c)−(d), show Rabi oscillations in the nonlinear regime (see green area in Fig.1b in the main text). At $\alpha^{in} = 5{\times}10^2\sqrt{\omega_m}$, Fig. 6c shows quasi-periodic behaviour, and at less three frequencies can be observed. In Fig. 6d however, several frequencies are involved, resulting in chaotic dynamics. To further characterize these dynamical states, we have used bifurcation diagram in frequency space (see Fig.3b in the main text). The reason lies on the difficulty of catching Rabi oscillation's dynamics in phase space. Indeed, Fig. 7a shows one period of Rabi oscillations with its corresponding phase space representation in the inset. Accordingly, this phase space trajectory features a set of limit cycles, each of those corresponds to each amplitude involved in the Rabi cycle [40]. Figs. 7(b)−(d) are the Fourier spectra corresponding respectively to regular ($\alpha^{in} = 4.5 \times 10^2\sqrt{\omega_m}$), quasi-periodic ($\alpha^{in} = 5 \times 10^2\sqrt{\omega_m}$) and chaotic Rabi oscillations ($\alpha^{in} = 5.5 \times 10^2\sqrt{\omega_m}$). The insets of these figures are the phase space representations, and they all feature a set of limit cycles as in Fig. 7a. It follows that, phase space representation is not a useful tool to distinguish between different dynamical states here. However, Fourier spectra in Figs. 7(b)−(d) clearly discriminate the dynamical states involved. Hence, varying the driving α^{in} at a fixed $J = 2.2 \times 10^{-2}\omega_m$, we were able to construct Fig.3b of the main text from Fast Fourier Transform (FFT).

Appendix B: Analytics

In the limit cycles regime, the amplitudes of the mechanical oscillations change only slowly over time (see Fig. 6b). Thus, we solve the equation for α_j assuming a fixed amplitude for the mechanical oscillations, and then use the result to solve the equation for β_j [41], [35]. Under this assumption, the mechanical oscillation can be described by the ansatz,

$$\beta_j(t) = \bar{\beta}_j + A_j \exp(-i\omega_{lock}t), \tag{B1}$$

where $\bar{\beta}_j$ is a constant shift in the origin of the resonator and the amplitude A_j is taken to be a slowly varying function of time. In such a weak coupling regime, we have denoted the locked frequency by ω_{lock}. We substitute this ansatz into the equation for α_j, and use the assumption of a slowly evolving amplitude to solve it, first neglecting the time dependence of A_j [35], [41]. We then obtain the intracavity field in the form,

$$\alpha_j(t) = e^{-i\theta_j(t)} \sum_n \alpha_n^j e^{in\omega_{lock}t}. \tag{B2}$$

The phase is $\theta_j(t) = -\epsilon_j \sin\omega_{lock}t$ and the amplitudes of the different harmonics of the optical field are,

$$\alpha_n^j = -i\sqrt{\kappa_j}\alpha^{in}\frac{J_n(-\epsilon_j)}{h_n^j}, \tag{B3}$$

where $\epsilon_j = \frac{2g\mathrm{Re(A_j)}}{\omega_{lock}}$, $\tilde{\Delta}_j = \Delta_j + 2g\mathrm{Re}(\bar{\beta}_\mathrm{j})$, $h_n^j = i\left(n\omega_{lock} - \tilde{\Delta}_j\right) + \frac{\kappa}{2}$ and J_n is the Bessel function of the first kind of order n.

As we are interested in the regime of limit cycles of the resonators, a rotating wave approximation can be made in which we drop all the terms (in the mechanical dynamics) except the constant one and the term oscillating at ω_{lock}. Hence, we substitute Eq. (B2) in the equation for β_j (see Eq. (B1)) which, by equating constant terms, leads to the zero-frequency components,

$$\begin{cases} \bar{\beta}_1 = \frac{1}{\omega_{01} - i\frac{\gamma_m}{2}}\left(g\kappa\sum_n \frac{\left(\alpha^{in}J_n(-\epsilon_1)\right)^2}{|h_n^1|^2} + J\bar{\beta}_2\right), \\ \bar{\beta}_2 = \frac{1}{\omega_{02} - i\frac{\gamma_m}{2}}\left(g\kappa\sum_n \frac{\left(\alpha^{in}J_n(-\epsilon_2)\right)^2}{|h_n^2|^2} + J\bar{\beta}_1\right), \end{cases} \tag{B4}$$

that induce a shifts of the cavity frequencies,

$$\delta_j = 2g\mathrm{Re}(\bar{\beta}_\mathrm{j}). \tag{B5}$$

The equations of motion for the oscillating part of β_j are deduced from $\beta_r^j(t) = \beta_j(t) - \bar{\beta}_j \equiv A_j \exp(-i\omega_{lock}t)$ and read,

$$\begin{cases} \dot{\beta}_r^1(t) = -i\left(\omega_{01} + \delta\omega_1\right)\beta_r^1 - \frac{\gamma_m + \gamma_{opt}^1}{2}\beta_r^1 + iJ\beta_r^2 \\ \dot{\beta}_r^2(t) = -i\left(\omega_{02} + \delta\omega_2\right)\beta_r^2 - \frac{\gamma_m + \gamma_{opt}^2}{2}\beta_r^2 + iJ\beta_r^1 \end{cases} \tag{B6}$$

Here the optical spring effect $\delta\omega_j$ and the optical damping γ_{opt}^j coming both from the average dynamics of the cavity are given by,

$$\delta\omega_j = -\frac{2\kappa(g\alpha^{in})^2}{\omega_{lock}\epsilon_j}\mathrm{Re}\left(\sum_\mathrm{n}\frac{\mathrm{J_{n+1}}\left(-\epsilon_\mathrm{j}\right)\mathrm{J_n}\left(-\epsilon_\mathrm{j}\right)}{\mathrm{h_{n+1}^{j*}h_n^j}}\right), \tag{B7}$$

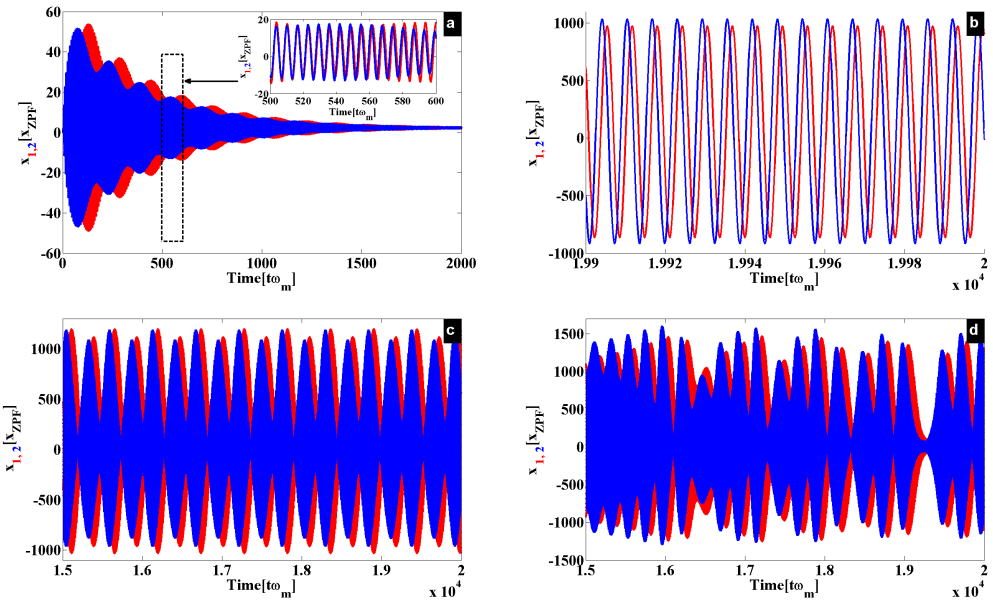

FIG. 6: Time propagations. (a) Fixed point state at $\alpha^{in} = 3 \times 10^2\sqrt{\omega_m}$. (b) Limit cycle state at $\alpha^{in} = 4.3 \times 10^2\sqrt{\omega_m}$. The corresponding spectrum and phase space trajectory are those of Fig.1c in the main text. (c) Quasi-periodic state at $\alpha^{in} = 5 \times 10^2\sqrt{\omega_m}$. (d) Chaotic state at $\alpha^{in} = 5.5 \times 10^2\sqrt{\omega_m}$. States (c) and (d) can be confirmed from the Lyapunov Exponent in the main text. The coupling strength is $J = 2.2 \times 10^{-2}\omega_m$ and the other parameters remain the same as in Fig.1 in the main text. Blue (red) color is related to the blue (red) mechanical supermode.

and

$$\gamma_{opt}^{j} = \frac{2(g\kappa\alpha^{in})^2}{\epsilon_j} \sum_n \frac{J_{n+1}\left(-\epsilon_j\right) J_n\left(-\epsilon_j\right)}{\left|h_{n+1}^{j*} h_n^j\right|^2}. \tag{B8}$$

For $\epsilon_j \ll 1$, the linear approximation is still valid and both the optical spring effect and the optical damping can be rewritten accordingly. Indeed, $\epsilon_j \ll 1$ induces $J_n\left(-\epsilon_j\right) \approx \frac{1}{n!}\left(\frac{-\epsilon_j}{2}\right)^n$ for $n \geq 0$ and $J_{-n}\left(-\epsilon_j\right) = J_n\left(\epsilon_j\right)$. Using these considerations in Eq. (B7) and Eq. (B8) yield,

$$\delta\omega_j\left(0\right) \approx -\frac{2\left(g_j\alpha_j^{in}\right)^2 \kappa_j\tilde{\Delta}_j\left[\frac{3\kappa_j^2}{4} + \left(\omega_{lock} - \tilde{\Delta}_j\right)\left(\omega_{lock} + \tilde{\Delta}_j\right)\right]}{\left(\frac{\kappa_j^2}{4}\left[\frac{\kappa_j^2}{4} + \left(\omega_{lock} - \tilde{\Delta}_j\right)\left(\omega_{lock} + \tilde{\Delta}_j\right)\right] - \kappa_j\tilde{\Delta}_j^2\right)^2 + \tilde{\Delta}_j^2\left[\frac{3\kappa_j^2}{4} + \left(\omega_{lock} - \tilde{\Delta}_j\right)\left(\omega_{lock} + \tilde{\Delta}_j\right)\right]^2}, \tag{B9}$$

$$\gamma_{opt}^{j}\left(0\right) \approx -\frac{\tilde{\Delta}_j\omega_{lock}\left(2g_j\kappa_j\alpha_j^{in}\right)^2}{\left(\tilde{\Delta}_j^2 + \frac{\kappa_j^2}{4}\right)\left[\left(\omega_{lock} + \tilde{\Delta}_j\right)^2 + \frac{\kappa_j^2}{4}\right]\left[\left(\omega_{lock} - \tilde{\Delta}_j\right)^2 + \frac{\kappa_j^2}{4}\right]}. \tag{B10}$$

These expressions are well in agreement with what is obtained in the linear regime [41], where both $\delta\omega_j$ and γ_{opt}^{j} are not amplitude dependent.

Appendix C: Effective Hamiltonian

From Eq.(B6), it is possible to define effective Hamiltonian in order to figure out supermodes involved in the system. Such supermodes will be deduced from the eigenmodes of the effective model, describing the mechanical

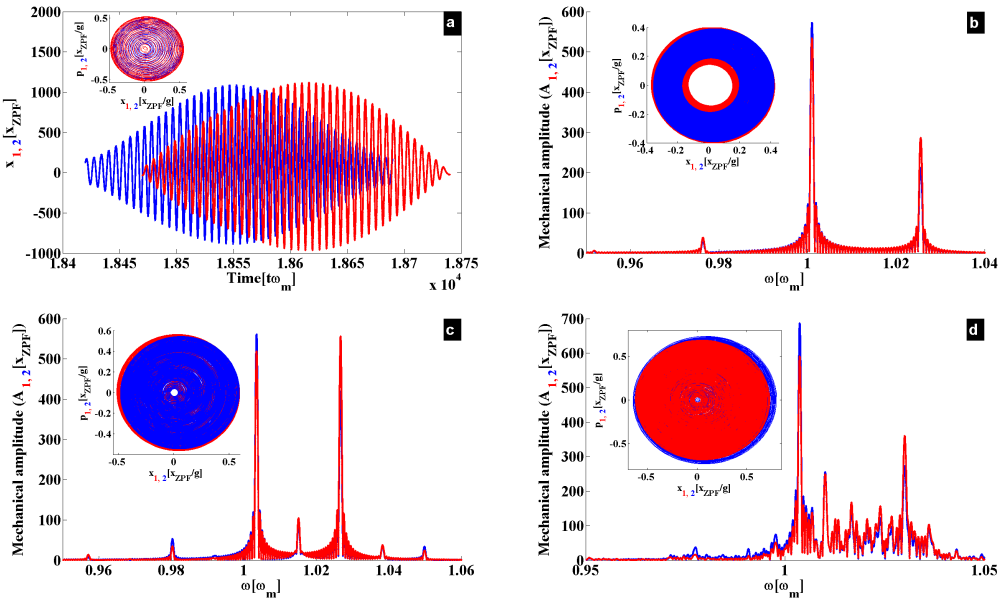

FIG. 7: Fourier spectra and phase space trajectories. (a) One Rabi cycle and the corresponding phase space, featuring a set of limit cycles. (b) Regular Rabi oscillations at $\alpha^{in} = 4.5 \times 10^2\sqrt{\omega_m}$. The corresponding time propagation is Fig.1d in the main text. (c) Quasi-periodic state corresponding to Fig. 6c, some satellite peaks can be observed. (d) Chaotic state corresponding to Fig. 6d, several peaks have emerged. Insets of these figures are their phase space trajectories, which all feature a set of limit cycles. Consequently, Fourier spectra are useful to distinguish these states, instead of the phase space representations. Blue (red) color is related to the blue (red) mechanical supermode.

resonators. Indeed, the real parts of the eigenmodes give the eigenfrequencies of the coupled system while their imaginary parts stand for the dissipations rate of the system. In the limit cycles regime, the constant shift $\bar{\beta}_j$ is weak compared to the amplitude of the mechanical resonator ($\bar{\beta}_j \ll A_j$). This means that $\beta_j(t) \cong \beta_r^j(t)$, and Eq.(B6) can be assumed as a set of equations describing the effective system that reads,

$$\begin{cases} \dot{\beta}_1 = -\left(i\omega_{eff}^1 + \frac{\gamma_{eff}^1}{2}\right)\beta_1 + iJ\beta_2, \\ \dot{\beta}_2 = -\left(i\omega_{eff}^2 + \frac{\gamma_{eff}^2}{2}\right)\beta_2 + iJ\beta_1, \end{cases} \tag{C1}$$

where $\omega_{eff}^j = \omega_{0j} + \delta\omega_j$ and $\gamma_{eff}^j = \gamma_m \pm \gamma_{opt}^j$ define the effective frequencies and the effective damping, respectively.

Furthermore, Eq.(C1) can be rewritten in the compact form,

$$\partial t\Psi = -iH_{eff}\Psi \tag{C2}$$

with the effective Hamiltonian,

$$H_{eff} = \begin{bmatrix} \omega_{eff}^1 - i\frac{\gamma_{eff}^1}{2} & -J \\ -J & \omega_{eff}^2 - i\frac{\gamma_{eff}^2}{2} \end{bmatrix} \tag{C3}$$

and the state vector $\Psi = (\beta_1, \beta_2)^T$.

The eigenvalues of the Hamiltonian given in Eq.(C3) are obtained by solving the equation,

$$\det\left(H_{eff} - \lambda I\right) = 0, \tag{C4}$$

and that yields to the following eigenvalues λ_- and λ_+,

$$\lambda_\pm \simeq \frac{\omega_{eff}^1 + \omega_{eff}^2}{2} - \frac{i}{4}\left(\gamma_{eff}^1 + \gamma_{eff}^2\right) \pm \frac{\sigma}{2}. \tag{C5}$$

with $\sigma = \sqrt{4J^2 - \frac{\Delta\gamma_{eff}^2}{4}}$ and $\Delta\gamma_{eff} = \gamma_{eff}^1 - \gamma_{eff}^2$. The frequencies and the dissipations of the supermodes are given by the real and imaginary parts of $\lambda_\pm$, respectively

$$\omega_\pm = \mathrm{Re}\left(\lambda_\pm\right) \text{ and } \gamma_\pm = \mathrm{Im}\left(\lambda_\pm\right).$$

From Eq.(C5), we deduce whether the system is in strong coupling regime or not. Indeed, for $J > \frac{\Delta\gamma_{eff}}{4}$, σ is real and this induces two distinct frequencies,

$$\omega_\pm = \frac{\omega_{eff}^1 + \omega_{eff}^2}{2} \pm \frac{\sigma}{2} \tag{C6}$$

that are spectrally separated by

$$\sigma = \omega_+ - \omega_- = \sqrt{4J^2 - \frac{\Delta\gamma_{eff}^2}{4}}. \tag{C7}$$

This splitting modes is the sign of strong coupling between the resonators and σ is the frequency of Rabi oscillations that emerge. The mechanical resonators have the same damping $\gamma_{\pm} = \frac{-\left(\gamma^1_{eff}+\gamma^2_{eff}\right)}{4}$. However, for $J < \frac{\Delta\gamma_{eff}}{4}$, σ is imaginary and the resonators oscillate at the same frequency,

$$\omega_{\pm} = \frac{\omega^1_{eff} + \omega^2_{eff}}{2}, \tag{C8}$$

with two distinct dissipations,

$$\gamma_{\pm} = \frac{-\left(\gamma^1_{eff} + \gamma^2_{eff}\right)}{4} \pm \frac{\sigma}{2}. \tag{C9}$$

This corresponds to a regime where the mechanical resonators are weakly coupled. The phase transition between these two regimes happens at the exceptional point (**EP**), where $J = \frac{\Delta\gamma_{eff}}{4}$ that is equivalent to $\sigma = 0$. To demonstrate the feature of multiple **EPs**, we need to show that $\sigma = 0$ can leads to multiple solutions. For this purpose, let us remind that $\Delta\gamma_{eff} \equiv \Delta\gamma^j_{opt}$. Then, using Eq.(B8) in Eq.(C7), leads straightforwardly to understand that σ is amplitude-dependent through the Bessel functions. Due to these Bessel functions, $\sigma = 0$ oscillates. These oscillations of σ, depending on the system's parameters, induce multiple solutions of $\sigma = 0$, resulting in multiple **EPs** feature.

[1] M. Aspelmeyer, T. J. Kippenberg, and F. Marquardt, Rev. Mod. Phys. **86**, 1391 (2014).
[2] A. D. O Connell et *al.*, Nature (London) **464**, 697 (2010).
[3] J. D. Teufel et *al.*, Nature (London) **475**, 359 (2011); J. Chan et *al.*, ibid. **478**, 89 (2011).
[4] J. B. Clark, F. Lecocq, R. W. Simmonds, J. Aumentado, and J. D. Teufel, Nature (London) **541**,191 (2017).
[5] M. Bagheri, M. Poot, M. Li, W.P.H. Pernice and H.X. Tang, Nature Nanotechnology **6**, 726 (2011).
[6] M.-A. Lemonde, N. Didier, and A. A. Clerk, Nat. Commun. **7**: 11338 doi:10.1038/ncomms11338 (2016).
[7] R. Leijssen, G. R. L. Gala, L. Freisem, J. T. Muhonen, and E. Verhagen, Nat. Commun. **8**: 16024 doi:10.1038/ncomms16024 (2017).
[8] C. Metzger, M. Ludwig, C. Neuenhahn, K. Karrai, A. Ortlieb, and F. Marquardt, Phys. Rev. Lett. **101**, 133903 (2008).
[9] F. M. Buters et *al.*, Phys. Scr. **T165**, 014003 (2015).
[10] D. Navarro-Urrios et *al.*, J. Opt. **18**, 094006 (2016); Sci. Rep. **5**, 15733 (2015).
[11] M. Zhang, G. S. Wiederhecker, S. Manipatruni, A. Barnard, P. McEuen, and M. Lipson, Phys. Rev. Lett. **109**, 233906 (2012).
[12] M. Bagheri, M. Poot, L. Fan, F. Marquardt, and H. X. Tang, Phys. Rev. Lett. **111**, 213902 (2013).
[13] S. Y. Shah, M. Zhang, R. Rand, and M. Lipson, Phys. Rev. Lett. **114**, 113602 (2015).
[14] M. Zhang, S. Shah, J. Cardenas, and M. Lipson, Phys. Rev. Lett. **115**, 163902 (2015).
[15] E. Gil-Santos et *al.*, Phys. Rev.Lett. **118**, 063605 (2017).
[16] S. Bregni, Synchronization of Digital Telecommunications Networks (John Wiley, New York, 2002).
[17] S. Strogatz, Sync: The Emerging Science of Spontaneous Order (Hachette Books, New York, 2003).
[18] T. B. Bahder, Clock Synchronization and Navigation in the Vicinity of the Earth (Nova Science, Hauppauge, 2009).
[19] I. Mahboob and H. Yamaguchi, Nat. Nanotechnol. **3**, 275 (2008).
[20] T. Carmon, M. C. Cross, and K. J. Vahala, Phys. Rev. Lett. **98**, 167203 (2007).
[21] F. Monifi, J. Zhang, Ş.K. Özdemir, B. Peng, Y.-X. Liu, F. Bo, F. Nori, and L. Yang, Nature Photonics **10**, 399 (2016).
[22] D. Navarro-Urrios et *al.*, Nat. Commun. **8**, 14965 doi: 10.1038/ncomms14965 (2017).
[23] L. Bakemeier, A. Alvermann, and H. Fehske, Phys. Rev. Lett. **114**, 013601 (2015).
[24] M. Sciamanna, and K. A. Shore, Nature Photonics. **9**, 151 (2015).
[25] X.-Y. Lü, H. Jing, J.-Y. Ma, and Y. Wu, Phys. Rev. Lett. **114**, 253601 (2015).
[26] M. Wang et *al.*, Sci. Rep. **6**, 22705 (2016).
[27] W. D. Heiss, J. Phys. A **37**, 2455 (2004).
[28] T. Goldzak, A. A. Mailybaev, and N. Moiseyev, Phys. Rev. Lett. **120**, 013901 (2018).
[29] B. Peng et *al.*, Science **346**, 328 (2014).
[30] J. D. Cohen et *al.*, Nature **520**, 522 (2015).
[31] S. Hong et *al.*, Science **358**, 203 (2017).
[32] C. M. Bender, B. K. Berntson, D. Parker, and E. Samuel, Am. J. Phys. **81**, 173 (2013).
[33] X.-W. Xu, Y.-X. Liu, C.-P. Sun, and Y. Li, Phys. Rev. A **92**, 013852 (2015).
[34] K. Ding, G. Ma, M. Xiao, Z. Q. Zhang, and C.T. Chan, Phys. Rev. X **6**, 021007 (2016).
[35] F. Marquardt, J. G. E. Harris, and S. M. Girvin, Phys. Rev. Lett. **96** , 103901 (2006).
[36] D. Platou Foulla, P. Djorwe, S. Takougang Kingni, and S. G. Nana Engo, Phys. Rev. A **95**, 013831 (2017).
[37] S. Zhang, Z. Yong, Y. Zhang, and S. He, Sci. Rep. **6**, 24487 (2016).
[38] J. Zhang et *al.*, Phys. Rev. B **92**, 115407 (2015).
[39] G. Wang, Y.-C. Lai, and C. Grebogi, Sci. Rep. **6**, 35381; doi: 10.1038/srep35381 (2016).
[40] X.-Y. Lü, H. Jing, J.-Y. Ma, and Y. Wu, Phys. Rev. Lett. **114**, 253601 (2015).
[41] D. A. Rodrigues, and A. D. Armour, Phys. Rev. Lett. **104**, 053601 (2010).